ORTHO-IMAGE OR NORMALIZED GEOSTATIONARY PROJECTION: WHICH PROJECTION IS BETTER FOR COMPARING THE REFLECTANCE OF GEO AND LEO SENSORS?

Masayuki Matsuoka*[1], Hiroki Yoshioka[2] and Kazuhito Ichii[3]
[1]Associate Professor, Graduate School of Engineering, Mie University
1577 Kurimamachiya, Tsu, Mie 514-8507 Japan
Email: matsuoka@info.mie-u.ac.jp

[2] Professor, Department of Information Science and Technology, Aichi Prefectural University
1522-3 Ibara-Gabasama, Nagakute, Aichi 480-1198 Japan

[3] Professor, Center for Environmental Remote Sensing, Chiba University
1-33, Yayoi-cho, Inage-ku, Chiba 263-8522 Japan

KEYWORDS: Geometric registration, Geostationary satellite, Polar-orbiting satellite, Spectral reflectance, Topographic effect

ABSTRACT: Simultaneous use of the geostationary orbit (GEO) sensor and low Earth orbit (LEO) sensor gives new perspective to Earth observation. This study evaluated the impact of the difference of image projection to the relationship of GEO and LEO reflectances using Himawari/AHI and Sentinel-2/MSI. Both data were reprojected to the Universal Transverse Projection and the normalized geostationary projection, respectively, and GEO and LEO reflectances were compared between two image projections. The results showed that the difference of image projection had relatively smaller impact compared with the difference of the observation geometry. Nevertheless, the reflectance difference in near-infrared band was approximately 0.1 at maximum in case of low solar elevation and mountainous terrain. It should be taken into consideration when making comparisons of GEO and LEO applications.

1. INTRODUCTION

1.1 Motivation

New generation geostationary orbit (GEO) sensors such as Himawari/AHI, GEO-KOMPSAT/AMI, and FengYun-4/AGRI, have observed the Asian region. Thanks to the their higher performance compared to previous meteorological sensors, simultaneous use with low Earth orbit (LEO) sensors would help understand various Earth surface phenomena, such as meteorology, disasters, vegetation phenology, and climate change.

One important preprocess is the geometric registration of GEO and LEO data, because they have different observation geometries (Figure 1). There are two main approaches to overlaying the GEO and LEO data. One is to orthorectify both images. This approach is somewhat closer to the LEO sensor and the result is easy to overlay with other geoinformation. However, it forces significant geometric deformation of the GEO data, especially at locations with higher altitudes and far from the subsatellite point. The other approach is to reproject the LEO data into the normalized geostationary projection, which is the same projection as the GEO data. We can expect the difference between the two approaches to be small on flat land surfaces, but what about mountainous areas like Japan?

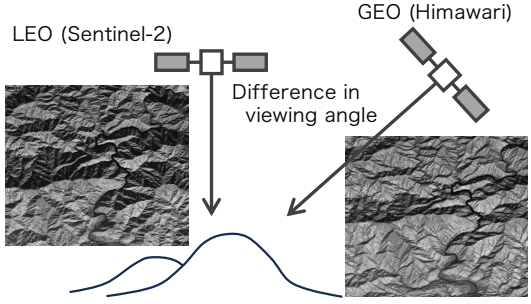

Figure 1. Difference in observation geometries between GEO and LEO satellites

1.2 Aims

This study aims to investigate the difference in reflectance between GEO and LEO sensors concerning two different image projections, map projection and satellite image projection. For map projection, orthorectification was applied to both GEO and LEO images to correct the parallax effect caused by the elevation. The satellite projection here is the normalized geostationary projection which describes the view from a virtual geostationary satellite to an idealized Earth (Coordination Group for Meteorological Satellites, 2013).

1.3 Related work

The integration of GEO and LEO sensors has been actively investigated in recent years. Miura et al. (2019) showed the advantage of hyper-temporal data of the GEO sensor to monitor the seasonal dynamics of vegetation and land surface. Hashimoto et al. (2021) compared the seasonality in greenness of the Amazon forests between the Advanced Baseline Imager (ABI) onboard the Geostationary Operational Environmental Satellite 16 (GOES-16) and the Moderate Resolution Imaging Spectroradiometer (MODIS). They showed that GEO data detected the seasonality of Amazon evergreen forest in the area three times greater than previously reported using LEO data. Adachi et al. (2019) developed the Relative Azimuthal-Angle Matching (RAM) as the screening for GEO-LEO reflectance comparison in the middle latitude forest where the observation geometries of GEO and LEO sensors significantly differ from those at low latitudes. For the inter-calibration of GEO and LEO sensors, Yu and Wu (2016) applied the Ray-matching method for evaluating the reflectance difference over the all-sky collocations with similar viewing and illumination geometries. The mutual utilization of high temporal GEO data and high spatial-resolution LEO data would advance the understanding of the Earth's environment.

The orthorectification method of GEO data has been investigated by several researchers. Yasukawa and Takagi (2003) reported the methodology of orthorectification of the Stretched-Visible and Infrared Spin Scan Radiometer (S-VISSR) onboard the Geostationary Meteorological Satellite-5 (GMS-5). Takeuchi et al. (2016) investigated the geometric accuracy of Himwari-8 and showed that geometric accuracy was greatly improved by an orthorectification process. Matsuoka and Yoshioka (2023) described the algorithm of orthorectification and applied it to Himawari/AHI, GOES-16/ABI, and FY-4/AGRI to evaluate the geometric error caused without orthorectification. The accurate registration of GEO and LEO data would be essential to improve the accuracy of remote sensing applications.

2. DATA

We used the Sentinel-2/MSI data for the LEO sensor because of its high observation frequency of five days and moderate spatial resolution of 10 m in visible and near-infrared (NIR) bands. Level 1C products were downloaded from Copernicus Open Access Hub (https://scihub.copernicus.eu). Map projection of level 1C product is the UTM projection, i.e., it is already orthorectified. For the GEO sensor, we used Himawari/AHI provided by the Japan Meteorological Agency (JMA). The data were downloaded via the NICT Science Cloud (https://sc-web.nict.go.jp/himawari/).

The study sites and the observation date of both sensors are listed in Table 1. We selected four sites in Japan considering the topography. Hokkaido and Kanto are mainly flat areas, but they contain the mountainous terrain in the surrounding area. Takayama and Kii Peninsula have rugged terrain with a series of mountains. For the observation date, we selected the four dates closest to the vernal equinox, summer solstice, autumnal equinox, and winter solstice as representative solar positions within the year, although they did not match perfectly due to cloud coverage. In addition to four Japanese sites, we adopted one site in Queensland, Australia because of its flatness. We also selected the two dates closest to the highest and the lowest solar elevations, and two dates between them. For Himawari data, we used the Japan Area data for Japanese sites, because their temporal resolution is 2.5 minutes, and it could reduce the time difference between Sentine-2 observations. For the Australian site, we used the Full Disk data that has a 10-minute temporal resolution.

Table 1. Observation dates of Himawari/AHI and Sentinel-2/MSI data

Location	Code	Observation date			
Hokkaido, Japan	HKD	3/30/2023	6/23/2021	9/11/2022	12/15/2022
Kanto, Japan	KNT	3/18/2021	7/1/2022	9/24/2021	12/18/2021
Takayama, Japan	TKY	3/31/2021	6/25/2019	9/28/2018	1/15/2021
Kii Peninsula, Japan	KII	3/21/2020	6/19/2023	10/2/2021	1/6/2020
Stokes, Australia	AUS	9/6/2022	11/05/2021	4/4/2023	6/18/2023

Figure 2(a) shows the Sentinel-2/MSI images in the UTM projection which were extracted from the level 1C products. Approximately half of the scenes contained small cloudy areas, but we masked them manually by visual interpretation to

exclude the cloud pixels from the analysis. Figure 2(b) shows the orthorectified Himawari/AHI images in the same sites as Sentinel-2. Due to the lower spatial resolution (i.e., 500 m in the red band, and 1 km in blue, green, and NIR bands), the images were low in spatial detail.

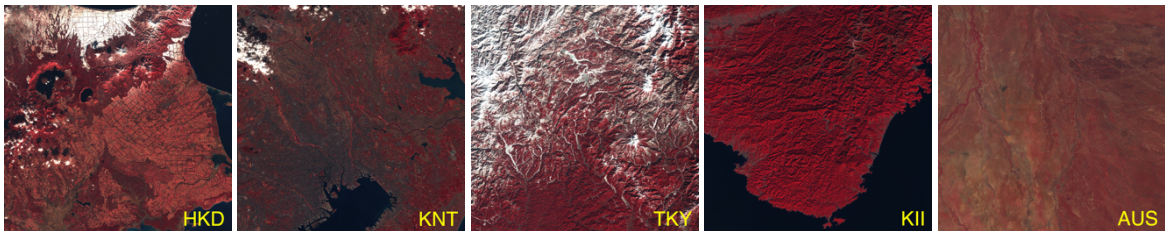

(a) Sentinel-2/MSI

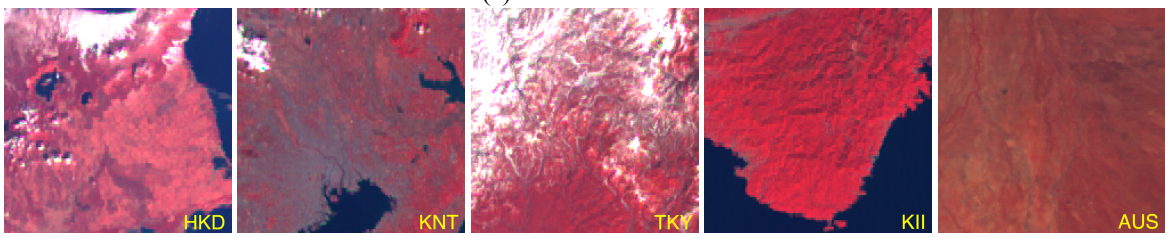

(b) Himawari/AHI

Figure 2. False-color images of five study sites in the UTM projection. The location codes are listed in Table 1. Observation dates are also listed in the last column of Table 1.

The land surface height from the Earth's ellipsoid is necessary for the reprojection of satellite data. We used the 10-m resolution Digital Elevation Model (DEM) and Japanese Geoid Model 2011 (v2.1) for the Japanese sites to calculate the height from an Earth ellipsoid. Both DEM and Geoid data were provided by the Geospatial Information Authority of Japan (GSI). For the Australia site, Global Multi-resolution Terrain Elevation Data 2010 (GMTED 2010, Danielson and Gesch, 2011) and the geoid height of Earth Gravitational Model 2008 (EGM2008, Pavlis et al., 2012) were used as elevation and geoid data, respectively.

3. METHOD

3.1 Reduction of the Geometric Error in Himawari/AHI Data

The JMA (2023a) reported that an accurate and stable geometric condition of the AHI can be achieved with a geometric accuracy of much less than 0.5 pixels for the bands whose nominal resolution is 2 km. To further improve the registration accuracy, we removed the bias error included in the AHI image by comparing it with the MSI image. The MSI band 4 (red) image was reprojected to the normalized geostationary projection with 50 m spatial resolution (the reprojection method is described in sections 3.2 and 3.3), and it was used as the reference image. The same area of the AHI image in band 3 was extracted from the original data and enlarged to the same spatial resolution as the reference MSI image. These images were divided into subgrids, and correspondent image positions were determined on a subgrid basis by sifting the AHI image on the MSI image. The position with the highest image correlation was adopted as the correspondent location. After the manual screening of error, a single pair of pixel shifts in horizontal and vertical directions was calculated for each observation date. AHI image was shifted based on this bias compensation value during the registration with MSI image.

3.2 Reprojection to the UTM Projection

Orthorectification based on the ray-tracing indirect method (Matsuoka et al. 2023) was applied to convert the Himawari/AHI image from the normalized geostationary projection to the UTM projection. The process steps were as follows:

1. Pixel position $(l, c)_U$ in the output image frame was converted to latitude and longitude $(\varphi, \lambda)_L$ based on the map projection parameters.
2. Ellipsoidal height $(h)_L$ at the location $(\varphi, \lambda)_L$ was extracted from the ellipsoidal height data.
3. The coordinate $(\varphi, \lambda, h)_L$ was converted to $(x, y, z)_L$ in the Earth-centered, Earth-fixed (ECEF) coordinate system.
4. The line of sight (LOS) vector was calculated using $(x, y, z)_L$ and the location of Himawari satellite in ECEF coordinate $(x, y, z)_S$.
5. The intersection of the LOS vector and the Earth ellipsoid $(x, y, z)_E$ was calculated.

6. The intersection $(x, y, z)_E$ was converted to the pixel position in AHI image $(l, c)_N$ in the normalized geostationary projection using a conversion program provided by JMA (2023b).

The output image frame was the same projection as the Sentinel-2/MSI, but spatial resolutions were 500 m for band 3 and 1 km for bands 1, 2, and 4 to match the AHI nominal resolutions. On the other hand, Sentinel-2/MSI data are originally in the UTM projection, therefore, we only decreased the spatial resolution from 10 m to the same resolutions as the above-mentioned AHI data.

3.3 Reprojection to the Normalized Geostationary Projection

To overlay with the Himawari/AHI image, the Sentinel-2/MSI image was converted from the UTM projection to the normalized geostationary projection as the same procedure described in Section 3.2. Many MSI pixels fall into a single AHI pixel because we applied this conversion to the original MSI image in 10 m resolution. The output reflectance was calculated by averaging these MSI pixels. In averaging, the cosine of the angle between the LOS vector and the normal vector of the land surface (derived by DEM) was used as the weight which indicates the apparent area observed by AHI. Finally, we masked the pixels at the edge of the MSI image because those pixels do not have enough number of pixels for averaging. For Himawari/AHI, we only cropped the same area as the converted MSI image.

3.4 Comparison of MSI and AHI Reflectances Between Two Projections

We compared the relationships of MSI and AHI reflectances between the UTM projection and the normalized geostationary projection. It was evaluated by the scatter plots and linear regression. In this evaluation, pixels of cloud, shadow, and ocean were masked to reduce the contamination. Viewpoints were as follows:

1. Does the image projection make a difference in reflectance relation?
2. Is there a clear topographic trend in reflectance relation?
3. Is there a clear seasonal trend in reflectance relation?

4. RESULTS AND DISCUSSION

4.1 Reflectances in the UTM Projection

The false-color images of Sentinel-2/MSI and Himawari/AHI in the UTM projection are shown in Figure 2. AHI images have higher reflectance (blighter images) than MSI, although the data were not atmospherically corrected and the spectral response functions of MSI and AHI were not the same. This is mainly due to the differences in viewing angle; MSI observes almost nadir, but AHI observes from the orbit above the equator. The reflectance difference looked larger in the mountainous areas such as TKY, KII, and the western part of HKD. The orthorectification was applied to these data, nevertheless, there were large differences between GEO and LEO reflectances. The GEO sensor observes a relatively larger fraction of the sunlit areas even on the flat plane, and it is more noticeable in mountainous terrain.

4.2 Reflectances in the Normalized Geostationary Projection

Figure 3 shows the false-color images in the normalized geostationary projection that provide the same view of the Earth as observed by the GEO sensor. Due to the geographic distortion by central projection, the same area (100 km ×

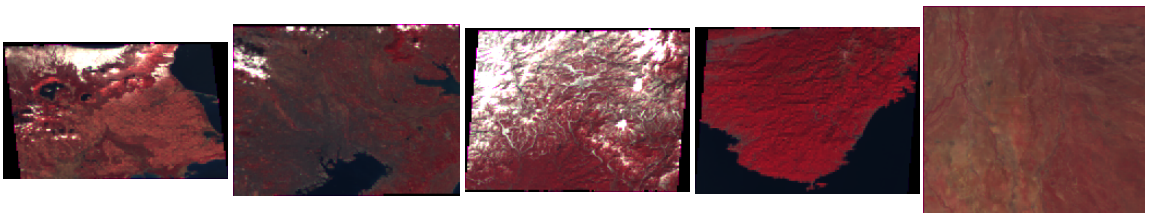

(a) Sentinel-2/MSI

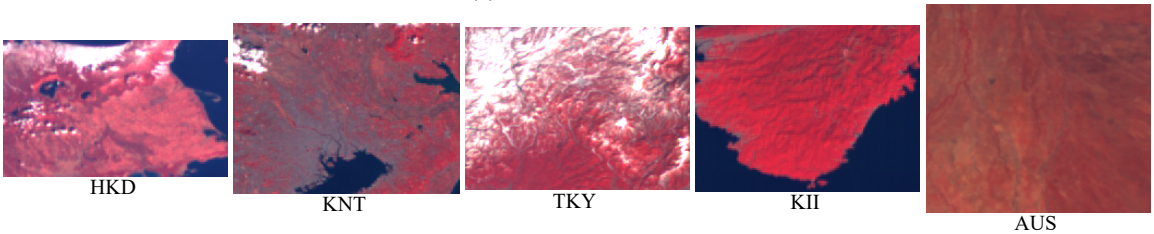

(b) Himawari/AHI

Figure 3. False-color images in the normalized geostationary projection. Sites and dates are the same as in Figure 2.

100 km) was converted to different image sizes. The blank areas, shown in black on the edge of the MSI images, were removed from the comparison. Although the image shapes were different from the UTM projection, the reflectance was almost the same, that is, AHI had higher reflectance than MSI, especially in mountainous areas.

4.3 Comparison of Reflectance

Comparisons of the scatter plots of MSI and AHI reflectances between the UTM projection and the normalized geostationary projection are shown in Figure 3. There were several interesting points listed below. For blue and green bands, we did not show the results because they were similar to those in red.

1. The UTM projection showed a broader distribution than the normalized geostationary projection. For example, yellow plots appeared surrounding the purple plots in the NIR band.
2. These differences were remarkable in the mountainous scenes such as TKY and KII, compared with flat areas such as KNT and AUS, especially in low solar-elevation season.
3. The difference between MSI and AHI reflectances was larger in the low solar-elevation season (near the winter solstice in Japan).

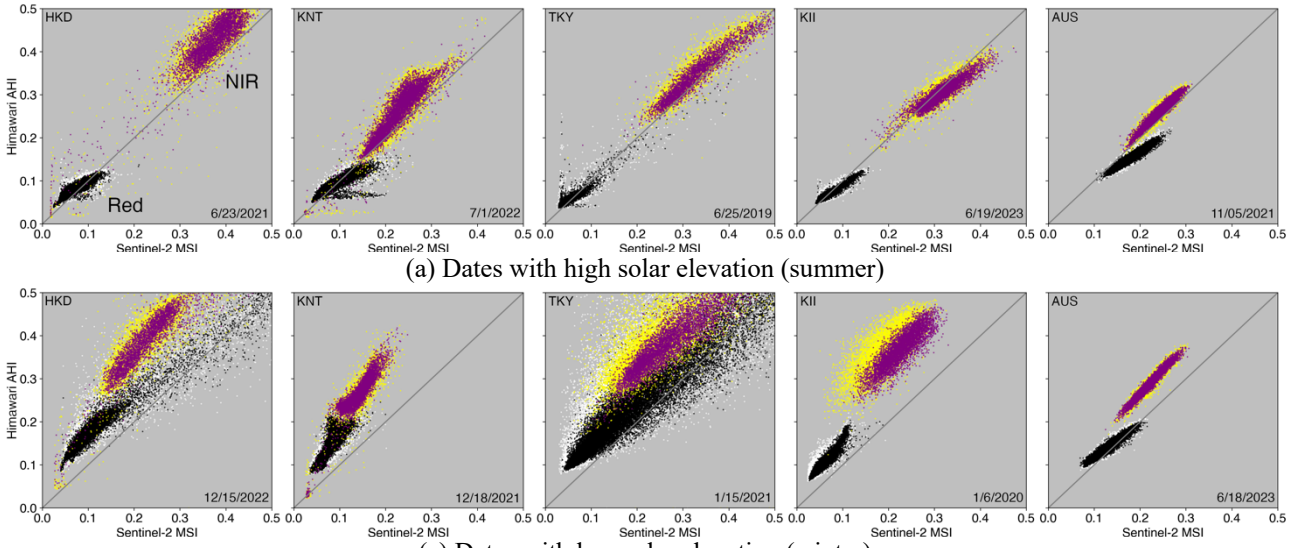

(a) Dates with high solar elevation (summer)

(a) Dates with low solar elevation (winter)

Figure 4. Comparison of the relations between Sentinel-2/MSI and Himawari/AHI reflectances. White and yellow plots show the red and NIR reflectance data in the UTM projection, respectively. Black and purple plots show the red and NIR reflectance data in the normalized geostationary projection, respectively.

4.4 Parameters and Residuals of the Linear Regression

We applied the linear regression of AHI reflectance by MSI reflectance in the UTM projection and showed the seasonal changes of the regression parameters (slope and intercept) in Figure 5. In red reflectance, HKD and TKY showed small slopes and large intercepts in high solar zenith angle (i.e., in winter) probably due to snow cover. For KNT and KII, the slopes increased along with the solar zenith angle, but intercepts were relatively stable, that is, the relations of MSI and AHI in red reflectance have proportional biases to the solar zenith angle rather than constant bias. In AUS, both slope and intercept were almost stable against the seasonal change in solar elevation. In NIR reflectance, seasonal changes in slope were smaller than those in red, although HKD and TKY indicated the decrease of slope in winter. Intercepts increased linearly with the solar zenith angle. These resulted in the constant biases shown in Figure 4.

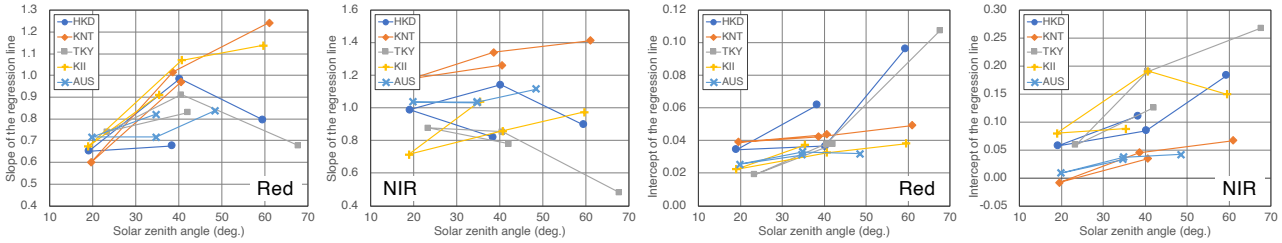

(a) Slope (b) Intercept

Figure 5. (a) slope and (b) intercept of the linear regression of AHI reflectance by MSI reflectance.

Figure 6 shows the seasonal changes in the root mean square of residuals (RMSRs) in the linear regression. The RMSRs were smaller in the normalized geostationary projection than those in the UTM projection in all sites and in all seasons. In the orthorectification of AHI, it is difficult to correct the terrain-affected reflectance, especially on the slope facing away from the satellite because the apparent area is smaller. This issue is considerable in the case of low-resolution GEO sensors. On the other hand, the reprojection of fine-resolution MSI image from the UTM projection to the normalized geostationary projection could adjust the apparent area of pixels by weighting the fraction of observable area. Therefore, GEO and LEO reflectances showed smaller discrepancies in the normalized geostationary projection.

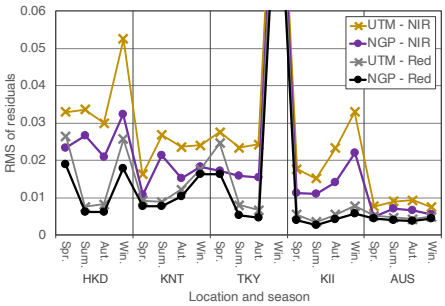

Figure 6. Root mean square of residuals in the linear regression of AHI reflectance by MSI reflectance.

The geographic view of the regression residual in the UTM projection is shown in Figure 7. Although HKD and TKY showed large residuals in snow areas, there were no clear trends in other land covers such as forest, urban, and agricultural areas. We also could not identify the topographic effect. In AUS, residuals were very small because of the flatness of land surface.

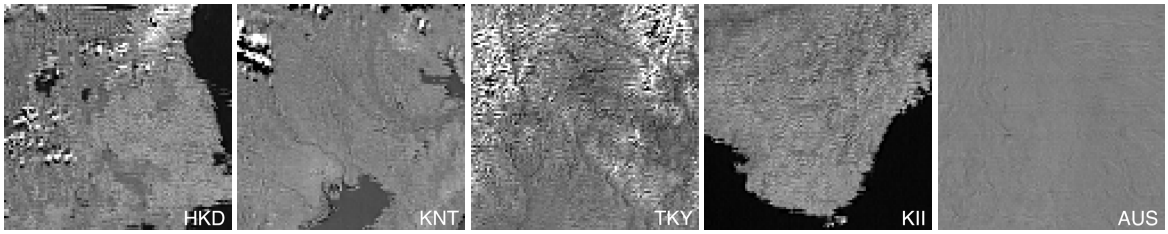

Figure 7. Geographic view of regression residuals in the UTM projection. The image brightness shows the residual range from −0.2 (black) to +0.2 (white). Images are in the NIR band in winter.

4.5 Discussion

From the comparison of GEO and LEO reflectance in Figure 4, we could identify that GEO reflectance is much higher than LEO reflectance especially in low solar-elevation mainly due to the difference in the observation geometry. In addition, the relation was dependent on the solar elevation and the topography. This difference in reflectance could cause discrepancies in the result of remote sensing applications such as land cover classification, energy budget calculations, and estimation of biogeophysical variables. Bidirectional reflectance modeling combining the GEO and LEO sensors probably can resolve these discrepancies.

The difference in image projection had a small impact on the disagreement of reflectances (RMSEs with roughly 0.01 in NIR and 0.001 in red reflectances respectively). Mountainous terrain enlarged this disagreement due to the variation of an apparent observed area associated with topography. Because GEO sensor observes the sunlit slope of terrain, the GEO reflectance tends to be higher than LEO reflectance in both map projection and satellite projection. It should be taken into consideration in the comparison of GEO and LEO applications.

5. CONCLUSIONS

The difference of GEO and LEO reflectances by image projection was analyzed using Himawari/AHI and Sentinel-2/MSI. The impact was relatively smaller compared to the impact of the bidirectional reflectance due to the difference in observation geometries of GEO and LEO sensors. Nevertheless, the reflectance difference was larger (up to approximately 0.1 in NIR) in case of lower solar elevation and in mountainous area. Further investigations would be focused on the modelling of bidirectional reflectances on mountainous terrain.

ACKNOWLEDGMENTS

This research was funded by the JSPS KAKENHI under grant numbers JP21K05669, JP20K20487, JP20KK0237, and JP22H05004. The authors would like to thank the Japan Meteorological Agency and the NICT Science Cloud for providing Himawari AHI Standard Data, and Copernicus Open Access Hub for providing Sentinel-2 MSI data.

REFERENCES

Adachi, Y., Kikuchi, R., Obata, K., Yoshioka, H., 2019, Relative Azimuthal-Angle Matching (RAM): A screening method for GEO-LEO reflectance comparison in middle latitude forests. *Remote Sens.,* 11(9), 1095. https://doi.org/10.3390/rs11091095

Coordination Group for Meteorological Satellites, 2013. LRIT/HRIT Global Specification (Issue 2.8). Available online: https://www.cgms-info.org/wp-content/uploads/2021/10/cgms-lrit-hrit-global-specification-(v2-8-of-30-oct-2013).pdf.

Danielson, J.J., Gesch, D.B., 2011. Global Multi-Resolution Terrain Elevation Data 2010 (GMTED2010). Available online: https://www.usgs.gov/publications/global-multi-resolution-terrain-elevation-data-2010-gmted2010

Hashimoto, H., Wang, W., Dungan, J.L., Li, S., Michaelis, A.R., Takenaka, H., Higuchi, A., Myneni, R.B., Nemani, R.R., 2021. New generation geostationary satellite observations support seasonality in greenness of the Amazon evergreen forests, *Nat. Commun.* 12, 684. https://doi.org/10.1038/s41467-021-20994-y

Matsuoka, M., Yoshioka, H., 2023. Orthorectification of data from the AHI aboard the Himawari-8 geostationary satellite. *Remote Sens.*, 15, 2403. https://doi.org/10.3390/rs15092403

Meteorological Satellite Center of Japan Meteorological Agency, 2023a. Himawari Series Satellite Image Navigation and Registration (INR). Available online: https://www.data.jma.go.jp/mscweb/data/monitoring/navigation.html

Meteorological Satellite Center of Japan Meteorological Agency. 2023b. Sample Source Code (C Programming Language). Available online: https://www.data.jma.go.jp/mscweb/en/himawari89/space_segment/spsg_sample.html

Miura, T., Nagai, S., Takeuchi, M., Ichii, K., Yoshioka, H., 2019. Improved characterization of vegetation and land surface seasonal dynamics in central Japan with Himawari-8 hypertemporal data. *Sci. Rep.*, 9, 15692. https://doi.org/10.1038/s41598-019-52076-x

Pavlis, N.K., Holmes, S.A., Kenyon, S.C., Factor, J.K., 2012. The development and evaluation of the Earth Gravitational Model 2008 (EGM2008). *J. Geophys. Res. Solid Earth*, 117, B04406. https://doi.org/10.1029/2011JB008916

Takeuchi, W., 2016. Assessment of geometric errors of Advanced Himawari-8 Imager (AHI) over one year operation. *IOP Conf. Ser.: Earth Environ. Sci.*, 37, 012004. https://doi.org/10.1088/1755-1315/37/1/012004

Yasukawa, M., Takagi, M., 2003. Geometric correction considering the elevation for GMS S-VISSR data. *J. Jpn. soc. photogramm. remote sens.*, 42(6), pp. 33-41. (In Japanese with English abstract) https://doi.org/10.4287/jsprs.42.6_33

Yu, F., Wu, X., 2016. Radiometric Inter-Calibration between Himawari-8 AHI and S-NPP VIIRS for the Solar Reflective Bands. *Remote Sens*., 8, 165. https://doi.org/10.3390/rs8030165